therapy. Function was checked before radiation therapy in 38 patients (61%), after radiation therapy in 32 (52%), and both before and after radiation therapy in 29 (47%). Six patients (10%) were checked only before radiation therapy. Device malfunction occurred in a patient (2%) with an ICP (Medtronic InSync; Medtronic Inc., Langhorne, PA) treated by intensity-modulated radiation therapy using 15 MV X-ray co-planar five ports dynamic multileaf collimator for prostate cancer. Total monitor units were 616 MU. He received a total dose of 74 Gy in 37 fractions. On a follow-up visit to his cardiologist, his ICP was found to have been initialized. From the ICP's memory, it was established that the initialization had occurred at doses of 46 Gy and 56 Gy. The device was interrogated and reprogrammed without any cardiac events except for mild fatigue. On the other hand, no malfunctions occurred in 6 patients whose absorbed doses were estimated to exceed 2 Gy.

ECG monitoring and consultation with cardiologist

Thirty-three patients (53%) did not undergo ECG monitoring during radiation therapy, but 13 patients (21%) underwent it every time they received a radiation treatment. Nine patients (5%) underwent ECG monitoring only on the first day of radiation therapy. Thirty-five patients (56%) were referred to a cardiologists and 24 (39%) were not.

DISCUSSION

The most common indication for placement of an ICP is the prevention of bradycardia and its resultant symptoms of syncope, near syncope, and cardiac arrest caused by sinus node dysfunction or atrio-ventricular block. A more recent indication is biventricular pacing in the treatment of congestive heart failure. During the past two decades, the devices have become smaller and the implantation procedure has become much less complicated. Furthermore, recent advances in the field of cardiology have improved the longevity of patients with acute myocardial infarction and heart failure. These developments have come from both the medical and technical arenas, with two trials demonstrating an advantage to the prophylactic use of ICDs.[3,4] These factors presumably will translate into the increased likelihood of these patients thriving despite their cardiac conditions. However, patients with and ICP/ICD who have cancer often will require radiation therapy, and such exposure may cause significant damage to ICPs and ICDs, with potentially life-threatening consequences. The cause of this damage may be the strong electromagnetic fields produced by linear accelerators, or the ionized radiation itself.

ICPs and ICDs can be affected by external electromagnetic fields. This may result in sensing the field as a myocardial potential, thus inhibiting its output.[5–7] Another malfunction is closing of the reed switch, which can result in fixed-rate pacing, triggering of output, or more serious functional impairment, including device reprogramming.[7] Fortunately, most interactions are reversible if the device is outside the radiation field. In contrast, ICP/ICD damage caused by ionizing radiation often is permanent and cumulative, and eventually will lead to failure of the device.[6–8]

Effective management guidelines are necessary for the safe use of radiation therapy. The first attempt at establishing such guidelines was published in 1989 in the informal venue of a newsletter from the American Society for Therapeutic Radiology and Oncology.[9] These recommendations were updated in 1994 by the AAPM TG-34,[1] but they did not include patients with ICDs. Several subsequent reports addressed the management of patients with ICPs or ICDs receiving radiation therapy.[7,10–12] For example, Solan *et al.*[10] made the following recommendations.

Patient management before initiation of radiation therapy

1. Identify patients with an ICP or ICD. Notify department personnel involved in direct patient care.
2. Determine whether the generator is located outside the direct, unshielded radiation therapy field, and if not, have the device moved.
3. Estimate the cumulative ionizing radiation dose to generator for dose estimates < 2 Gy for ICP or < 1 Gy for ICD.
4. Have the cardiologist determine whether the patient is pacemaker dependent or non-pacemaker dependent. Provide deactivation instructions for ICDs, and full baseline assessment of the ICP or ICD.

Patient management during radiation therapy

1. Do not treat with a betatron device.
2. Compare TLD or diode measurement of dose at first treatment with the pretreatment estimate to ensure that dose limits are met.
3. Ensure that patients are monitored by therapists during all treatments. Treating physicians should observe patients during initial portal imaging and during the first treatment. All patients should undergo measurement of pulse and blood pressure before and after each treatment. Pacemaker-dependent patients should have continuous ECG monitoring during their first treatment and a weekly ICP or ICD check by the cardiologist.
4. Use a magnet to deactivate the ICD before treatment if so advised by the cardiologist.

Patient management after completion of radiation therapy

1. Full assessment of ICP or ICD function by the cardiologist.

Modern multi-programmable ICPs and ICDs are very sen-

Table 3. Management of cases with ICPs or ICDs before, during and after radiation therapy

Correlation between devices and radiation field			
Outside radiation field during treatment	62	(100%)	
Inside radiation field during portal imaging	21	(34%)	
Estimated absorbed dose of devices			
By DVH	22	(35%)	highest dose 2069 cGy
By TLD or diode measurement and DVH	2	(3%)	highest dose 229 cGy
By phantom and DVH	2	(3%)	highest dose 185 cGy
By TLD or diode measurement	3	(5%)	highest dose 45 cGy
By phantom	2	(3%)	highest dose 8 cGy
No absorbed dose estimate	31	(50%)	
Check of device's function			
Did not check function	10	(16%)	
Checked function	52	(84%)	
Before radiation therapy	38	(61%)	
After radiation therapy	32	(52%)	
Before and after radiation therapy	29	(47%)	
Only before radiation therapy	6	(10%)	
Malfunction	1	(2%)	
ECG monitoring			
Did not ECG monitoring	33	(53%)	
Did ECG monitoring	29	(47%)	
Every time	13	(21%)	
Only first time	9	(5%)	
Consult cardiologist			
Did not consult cardiologist	24	(39%)	
Did consult cardiologist	35	(56%)	
Unknown	2	(3%)	

DVH: dose volume histogram
TLD: thermoluminescence dosimeter
ECG: electrocardiogram

ICP/ICD were estimated by dose-volume histogram (DVH) alone. The maximum dose was estimated at 2069 cGy, and the second-highest dose was estimated at 478 cGy. In 2 patients (3%), the absorbed radiation dose was estimated by thermoluminescence dosimeter (TLD) or diode measurement in addition to DVH, whose maximum dose was 229 cGy. Absorbed radiation doses also were estimated by both phantom and DVH in 2 patients (3%), whose maximum dose was 185 cGy; by TLD or diode measurement alone in 3 patients (5%), whose maximum dose was 45 cGy; and by phantom alone in 2 patients (3%), whose maximum dose was 8 cGy. The total dose absorbed by ICP/ICD was estimated by DVH in 26 patients (42%) and by measurement of actual doses in 9 patients (15%). For one patient, the maximum dose was 2069 cGy; however, it did not exceed 478 cGy in any other patient. For 6 patients, absorbed doses were estimated to exceed 2 Gy. In 31 cases (50%), absorbed doses were not estimated.

Assessment of device function

For 10 patients (16%), function of the ICP or ICD was not checked before, during, or after the completion of radiation

that the total dose does not exceed 2 Gy.
6. If this is not possible, have the device either temporarily or permanent moved.

However, these guidelines do not address the management of patients who have an ICD. Moreover, our previous study of policies for managing patients with ICPs or ICDs treated with radiation therapy showed a low level of expertise among major radiation departments throughout Japan.[2] Only 18 (17%) of 108 institutions estimated device exposure before radiation therapy and consulted a cardiologist, and only 19 centers (18%) performed electrocardiographic (ECG) monitoring. These concerns prompted us to conduct a prospective survey of patients with these devices who had received radiation therapy.

PATIENT AND METHODS

Ninety-six of the 223 major radiation oncology departments participated in the prospective survey. The survey comprised questions on the methods of radiation therapy, status of ICP or ICD, and management of patients before, during, and after radiation therapy. After completion of their radiation therapy, patients were registered for study participation via mail, fax, or e-mail.

From September 2006 to December 2008, a total of 62 patients (60 with an ICP, 2 with an ICD) from 29 institutions were registered (Table 1). The age range 58 to 89 years (median, 76). There were 44 males and 17 females. For one case, gender was not specified on the registration form. The reasons for the implanted device were atrio-ventricular block (n = 25), sick sinus syndrome (n = 23), atrial fibrillation (n = 5), ventricular fibrillation (n = 1), and other diseases (n = 8). The types of ICPs and ICDs are shown in Table 2.

Radiation therapy was carried out because of lung cancer (n = 15), prostate cancer (n = 7), esophageal cancer (n = 7), breast cancer (n = 4), head and neck cancer (n = 4), malignant lymphoma (n = 4), and other malignancies (n = 21). The total radiation dose ranged from 20 to 74 Gy (median, 50 Gy). Four patients were treated by stereotactic radiation therapy for lung cancer, and two were treated by stereotactic radiosurgery by CyberKnife (Accuray Inc., Sunnyvale, CA). Intensity-modulated radiation therapy was performed for a patient with prostate cancer.

RESULTS (Table 3)

Correlation between devices and the radiation field

In all patients, the ICP or ICD was located outside the treatment field. In 21 patients (34%), the device was inside the radiation field of portal images (18 irradiated to the chest, 3 to the head and neck).

Estimated dose absorbed by the devices

For 22 patients (35%), the radiation doses absorbed by the

Table 1. Patients characteristics

Devices		
ICPs		60
ICDs		2
Age		
58–89 years old, median 76 (unknown 3)		
Gender		
Male		44
Female		17
Unknown		1
Cardiovascular disease		
Atrio-ventricular block	25	
Sick sinus syndrome		23
Ventricular fibrillation		1
Atrial fibrillation		5
Others		8
Disease treated by radiation therapy		
Lung cancer		15
Prostate cancer	7	
Esophageal cancer		7
Breast cancer		4
Head and Neck cancer	4	
Malignant lymphoma		4
Others		21
Total radiation dose		
20–74 Gy, median 50 Gy		

ICPs: Implanted cardiac pacemakers
ICDs: Implantable cardio-defibrillators

Table 2. Types of implanted cardiac pacemakers (ICP) and implantable cardioverter defibrillators (ICDs)

ICP or ICD	Manufacturer	Type
ICD	Medtronic	GEM 2
ICP	Medtronic	Insync 1, EnPulse 2, Kappa 12, Sensia 1, Unknown 1
	St Jude	Fidelity 6, Identity 3, Integrity 3, Verity 1, Regency 5, Affinity 5, unknown 1
	Biotronic	Actros 2, Philos 4
	GuidantDiscovery 2	
	Intermedics	Nexus 2, Virtus 1
	Ela Medical	Symphony 2
	Vitatron	Clanity 1, Diamond 1
	Unknown 4	

J. Radiat. Res., 52, 516–521 (2011)

Regular Paper

Radiation Therapy in Patients with Implanted Cardiac Pacemakers and Implantable Cardioverter Defibrillators: A Prospective Survey in Japan

Toshinori SOEJIMA[1]*, Eisaku YODEN[2], Yasumasa NISHIMURA[3], Seiji ONO[4], Akihiro YOSHIDA[5], Haruyuki FUKUDA[6], Noboru FUKUHARA[7], Ryohei SASAKI[8], Kayoko TSUJINO[1] and Yoshiki NORIHISA[9]

Radiotherapy/Pacemaker/ICD/Malfunction.

Patients with implanted cardiac pacemakers (ICPs) or implantable cardioverter defibrillators (ICDs) are increasing in number, and the incidence of treating these patients with radiation therapy also is increasing. Thus, a prospective survey was conducted of patients with these devices receiving radiation therapy. A prospective survey of patients with ICPs or ICDs treated with radiation therapy was conducted on methods of radiation therapy, status of ICP/ICD, and management of patients before, during, and after radiation therapy. After completion of radiation therapy, study participants were registered via mail, fax, or e-mail. Sixty-two patients from 29 institutions were registered from September 2006 to December 2008. Sixty patients had an ICP and 2 had an ICD. The total dose was estimated before radiation therapy by dose-volume histogram in 26 patients (42%) and by measurement of actual doses in 9 (15%). In one patient, the maximum total dose was 2069 cGy; however, in the other patients, the ICP/ICD dose did not exceed 478 cGy. Function of ICPs and ICDs was checked before radiation therapy in 38 patients (61%), after radiation therapy in 32 (52%), and both before and after radiation therapy in 29 (47%). ICP malfunction occurred in a patient with prostate cancer treated by intensity-modulated radiation therapy to the prostate. Even when an ICP or ICD is not within the field of radiation, malfunction of the device may still occur. To minimize the risk to patients, precautions must be taken during the planning and administration of radiation therapy.

INTRODUCTION

Patients with implanted cardiac pacemakers (ICPs) or implantable cardioverter defibrillators (ICDs) are increasing in number, and the incidence of treating these patients with radiation therapy also is on the rise. Although the risk of potentially life-threatening malfunction owing to electromagnetic interference or ionizing radiation is well known, the proper management of patients with ICPs or ICDs by radiation oncologists has not been clearly defined. In Japan, there have been no practical guidelines for managing patients with an ICP or ICD treated with radiation therapy. The American Association of Physicists in Medicine Task Group-34 (AAPM TG-34) established management guidelines for patient with ICPs in 1994,[1)] which are summarized below.

1. Ensure that the patient's coronary and device status is assessed by a cardiologist before and soon after the completion of radiation therapy.
2. Never treat a patient with a betatron device.
3. Keep the device outside the collimated radiation beam, during both treatment and portal imaging.
4. Observe the patient during the first fraction of treatment to ensure that no transient malfunctions occur.
5. Estimate and record the absorbed dose received by the device before treatment. Position the fields so

*Corresponding author: Phone: +78-929-1151,
Fax: +78-929-2380,
E-mail: soe@hp.pref.hyogo.jp

[1]Department of Radiation Oncology, Hyogo Cancer Center, 13-70 Kitaoujicho, Akashi, 673-8558, Japan; [2]Department of Radiation Oncology, Kawasaki Medical School, 577 Matsushima, Kurashiki, 701-0192, Japan; [3]Department of Radiation Oncology, Kinki University Faculty of Medicine, 377-2 Oono-higashi, Osaka-sayama, 589-8511, Japan; [4]Kyushu University of Health and Welfare, 1714-1 Yoshino-cho, Nobeoka, 882-8508, Japan; [5]Division of Cardiovascular and Respiratory Medicine, Kobe Graduate University School of Medicine, 7-5-2 Kusunoki-cho, Chuo-ku, Kobe, 650-0017, Japan; [6]Department of Radiation Oncology, Osaka Saiseikai Nakatsu Hospital, 2-10-39 Shibata, Kita-ku, Osaka, 530-0012, Japan; [7]Department of Radiology, Sagamihara Kyodo Hospital, 2-8-18 Hashimoto, Midori-ku, Sagamihara, 252-5188, Japan; [8]Division of Radiation Oncology, Kobe Graduate University School of Medicine, 7-5-2 Kusunoki-cho, Chuo-ku, Kobe, 650-0017, Japan; [9]Department of Radiation Oncology and Image-applied Therapy, Kyoto University Graduate School of Medicine, 54 Kawahara-cho, Shogoin, Sakyo-ku, Kyoto, 606-8507, Japan.
doi:10.1269/jrr.10143

[23] Ozaki H, Hiraoka T, Mizumoto R, et al. The prognostic significance of lymph node metastasis and intrapancreatic perineural invasion in pancreatic cancer after curative resection. Surg Today 1999;29:16–22.
[24] Loehrer PJ, Powell ME, Cardenes HR, Wagner L, Brell JM, Ramanathan RK, et al. Eastern Cooperative Oncology Group. A randomized phase III study of gemcitabine in combination with radiation therapy versus gemcitabine alone in patients with localized, unresectable pancreatic cancer: E4201. J Clin Oncol 2008;26 [May 20 Suppl.; abstr 4506].
[25] Schulz.-Ertner D, Tsujii H. Particle radiation therapy using proton and heavier ion beams. J Clin Oncol 2007;25:953–64.
[26] Shinchi H, Takao S, Noma H, et al. Length and quality of survival after external-beam radiotherapy with concurrent continuous 5-fluorouracil infusion for locally unresectable pancreatic cancer. Int J Radiat Oncol Biol Phys 2002;53:146–50.
[27] Sohn TA, Yeo CJ, Cameron JL, et al. Resected adenocarcinoma of the pancreas-616 patients: results, outcomes, and prognostic indicators. J Gastrointest Surg 2000;4:567–79.
[28] Vincent A, Herman J, Schulick R, Hruban RH, Goggins M. Pancreatic cancer. Lancet 2011;378:607–20.
[29] Wong D, Ko AH, Hwang J, Venook AP, Bergsland EK, Tempero MA. Serum CA19-9 decline compared to radiographic response as a surrogate for clinical outcomes in patients with metastatic pancreatic cancer receiving chemotherapy. Pancreas 2008;37:269–74.

the patients died of local progression. One patient (2%) who developed both locoregional and distant metastases died of gastric hemorrhage (grade 5). Twelve patients (24%) have survived over 12 months to date without any signs of local or distant tumor progression.

Discussion

Our study indicated the high feasibility and tolerability of proton radiotherapy concurrently with high dose gemcitabine at 800 mg/m^2 on days 1, 8, and 15 during proton beam radiotherapy. The low frequency of grade 3 or greater acute GI toxicities, even at doses as high as 70.2 GyE (P-2) or 67.5 GyE (P-3), suggests superior dose localization of the proton beams to the target. However, late GI toxicities in P-3 (gastric ulcer and hemorrhage of grade 5) cannot be disregarded. We recognized that gastric peristalsis might bring unexpected high dose to the stomach, leading to severe complications in those patients, but it is a limitation of the current treatment planning technique. To prevent these major late toxicities, we have restricted irradiation doses to the GI tract by regulating the target fields and gantry angles and selecting an optimal split dose for the field-within-a-field technique. In contrast to the gastric toxicities, we did not encounter critical ulcer or hemorrhage in the duodenum, although it was irradiated at a dose similar to that of the stomach. The reason that no serious GI toxicity occurred in patients with pancreatic body/tail cancer seems to stem from the tolerability of the duodenum. As this lower frequency of duodenal toxicity is very interesting, we continued careful observation of the duodenum by duodenal fiberscopy.

From our clinical experience, it appears that the field-within-a-field technique that we used at P-3 enabled us to reduce the irradiation of OAR while maintaining the necessary doses to the PTV. Our analyses of the DVH indicate that using the field-within-a-field technique can increase the dose to the PTV of patients with GI-adjacent LAPC. Despite an increase in the dose to the PTV, the maximum dose to the stomach and duodenum was not increased. In addition, the optimal split dose of the field-within-a-field technique can be selected according to the tumor adjacency to the GI tract, so that the OAR are irradiated within a tolerable limit. Accordingly, GPT performed using the field-within-a-field technique contributed to solving of the mentioned three problems: reduction of irradiation dose, gemcitabine dose, and irradiation field.

Murphy et al. demonstrated that FFLP was a significant factor of OS on multivariate analysis [20]. To improve FFLP, our GPT was designed to deliver proton beams at a higher dose to a large CTV with concurrent administration of gemcitabine. As a result, the one-year FFLP and OS rates in our study were greater than expected, with high rates of 81.7% and 76.8%, respectively. This high FFLP rate is considered to be due to a large CTV, which was locally irradiated by proton beams at a high dose; thus, a good OS rate was achieved with low toxicities. However the one-year PFS rate was 64.3% which is low compared with the high FFLP and OS rates, this PFS rate is apparently better than that of other treatment modalities for patients with LAPC. Namely, the reported PFS rates are approximately 10–20% for CRT [7,17,22] and 10–15% for gemcitabine-based chemotherapy alone [1,9]. It is likely that the substantial local control of the primary tumor exerted by GPT decreased distant metastases and that the use of concurrent and adjuvant gemcitabine has contributed to the prolongation of life of patients with LAPC.

The one-year OS rate obtained in our study is apparently better than that obtained for patients treated with chemo-photon therapy [7,17,20]. Therefore, we consider that proton therapy using the field-within-a-field technique combined with concurrent gemcitabine or another promising chemotherapy has the potential to improve survival, including radical cure, for patients with LAPC.

Conclusions

GPT for LAPC was feasible and tolerable, and GPT using the field-within-a-field technique resulted in high FFLP and OS rates in our study. Although the number of patients enrolled in this study is too small and the follow-up periods are too short to draw any definitive conclusions, the clinical results obtained to date seem very encouraging.

Conflicts of interest

None.

References

[1] Burris 3rd HA, Moore MJ, Andersen J, et al. Improvements in survival and clinical benefit with gemcitabine as first-line therapy for patients with advanced pancreas cancer: a randomized trial. J Clin Oncol 1997;15:2403–13.
[2] Carpelan-Holmstrom M, Nordling S, Pukkala E, et al. Does anyone survive pancreatic ductal adenocarcinoma? A nationwide study re-evaluating the data of the Finnish Cancer Registry. Gut 2005;54:385–7.
[3] Casper ES, Green MR, Kelsen DP, et al. Phase II trial of gemcitabine (2,2′-difluorodeoxycytidine) in patients with adenocarcinoma of the pancreas. Invest New Drugs 1994;12:29–34.
[4] D'Souza MA, Shrikhande SV. Pancreatic resectional surgery: an evidence-based perspective. J Cancer Res Ther 2008;4:77–83.
[5] Galloway NR, Aspe JR, Sellers C, Wall NR. Enhanced antitumor effect of combined gemcitabine and proton radiation in the treatment of pancreatic cancer. Pancreas 2009;38:782–90.
[6] GITSG. Treatment of locally unresectable carcinoma of the pancreas: comparison of combined-modality therapy (chemotherapy plus radiotherapy) to chemotherapy alone. Gastrointestinal Tumor Study Group. J Natl Cancer Inst 1988;80:751–5.
[7] Huang PI, Chao Y, Li CP, et al. Efficacy and factors affecting outcome of gemcitabine concurrent chemoradiotherapy in patients with locally advanced pancreatic cancer. Int J Radiat Oncol Biol Phys 2009;73:159–65.
[8] Ikeda M, Okada S, Tokuuye K, Ueno H, Okusaka T. Prognostic factors in patients with locally advanced pancreatic carcinoma receiving chemoradiotherapy. Cancer 2001;91:490–5.
[9] Ishii H, Furuse J, Boku N, et al. Phase II study of gemcitabine chemotherapy alone for locally advanced pancreatic carcinoma: JCOG0506. Jpn J Clin Oncol 2010;40:573–9.
[10] Iwata H, Murakami M, Demizu Y, et al. High-dose proton therapy and carbon-ion therapy for stage I nonsmall cell lung cancer. Cancer 2010;116:2476–85.
[11] Kagawa K, Murakami M, Hishikawa Y, et al. Preclinical biological assessment of proton and carbon ion beams at Hyogo Ion Beam Medical Center. Int J Radiat Oncol Biol Phys 2002;54:928–38.
[12] Kamigaki T, Murakami M, Matsumoto IMM. A phase I study of proton beam therapy for locally advanced pancreatic cancer: analysis of feasibility and anti-tumor effect. J Clin Oncol 2008;26 [May 20 Suppl.; abstr 15675) 2008].
[13] Kavanagh BD, Pan CC, Dawson LA, et al. Radiation dose–volume effects in the stomach and small bowel. Int J Radiat Oncol Biol Phys 2010;76:S101–7.
[14] Kirkpatrick JP, van der Kogel AJ, Schultheiss TE. Radiation dose–volume effects in the spinal cord. Int J Radiat Oncol Biol Phys 2010;76:S42–9.
[15] Komatsu S, Fukumoto T, Demizu Y, et al. Clinical results and risk factors of proton and carbon ion therapy for hepatocellular carcinoma. Cancer 2011.
[16] Lawrence TS, Eisbruch A, McGinn CJ, Fields MT, Shewach DS. Radiosensitization by gemcitabine. Oncology (Williston Park) 1999;13:55–60.
[17] Li CP, Chao Y, Chi KH, et al. Concurrent chemoradiotherapy treatment of locally advanced pancreatic cancer: gemcitabine versus 5-fluorouracil, a randomized controlled study. Int J Radiat Oncol Biol Phys 2003;57:98–104.
[18] Moertel CG, Frytak S, Hahn RG, et al. Therapy of locally unresectable pancreatic carcinoma: a randomized comparison of high dose (6000 rads) radiation alone, moderate dose radiation (4000 rads + 5-fluorouracil), and high dose radiation + 5-fluorouracil: The Gastrointestinal Tumor Study Group. Cancer 1981;48:1705–10.
[19] Morganti AG, Valentini V, Macchia G, et al. 5-Fluorouracil-based chemoradiation in unresectable pancreatic carcinoma: phase I–II dose-escalation study. Int J Radiat Oncol Biol Phys 2004;59:1454–60.
[20] Murphy JD, Adusumilli S, Griffith KA, et al. Full-dose gemcitabine and concurrent radiotherapy for unresectable pancreatic cancer. Int J Radiat Oncol Biol Phys 2007;68:801–8.
[21] Nishimura H, Ogino T, Kawashima M, et al. Proton-beam therapy for olfactory neuroblastoma. Int J Radiat Oncol Biol Phys 2007;68:758–62.
[22] Okusaka T, Ito Y, Ueno H, et al. Phase II study of radiotherapy combined with gemcitabine for locally advanced pancreatic cancer. Br J Cancer 2004;91:673–7.

Table 2
Summary of proton therapy.

	P-1 50 GyE/25 fr Median (range), GyE	P-2 70.2 GyE/26 fr Median (range), GyE	P-3 67.5 GyE/25 fr Median (range), GyE	*t*-test (P-1, P-3) *P*-value	*t*-test (P-2, P-3) *P*-value
GTV $D_{80\%}$	49.9 (49.6–50)	58.2 (43.6–68.1)	53.4 (43.1–66.4)	<0.01	0.12
GTV $D_{50\%}$	50.2 (50–50.4)	64.4 (49.2–70.1)	61.1 (50.2–67.6)	<0.01	0.22
GTV $D_{20\%}$	50.6 (50.4–50.8)	66.6 (52.3–70.4)	66 (57.1–68.1)	<0.01	0.88
CTV $D_{80\%}$	49.9 (49.4–50.4)	56.1 (41.9–65.6)	52.5 (41.7–60)	<0.01	0.19
CTV $D_{50\%}$	50.3 (50–50.5)	64.4 (48.9–69.1)	62.6 (53.2–67.1)	<0.01	0.68
CTV $D_{20\%}$	50.7 (50.5–51)	66.6 (51.6–70.8)	67.4 (65.4–68.2)	<0.01	0.85
PTV $D_{80\%}$	49.7 (49.4–50.1)	51.6 (36.6–60.7)	49.4 (40.8–61)	0.72	0.42
PTV $D_{50\%}$	50.3 (50–50.5)	61.4 (46.2–67.6)	59.5 (46.3–66.5)	<0.01	0.50
PTV $D_{20\%}$	50.8 (50.6–51.2)	66.3 (50.8–70.4)	66.9 (63.1–68)	<0.01	0.89
Stomach D_{max}	51 (4–52)	46 (39–56)	48 (38–52)	0.52	0.54
Duodenum D_{max}	41 (40–46)	51 (51–52)	48.5 (42–52)	<0.01	<0.01

Abbreviations: GyE, gray equivalents; fr, fractions; GTV, gross tumor volume; CTV, clinical target volume; PTV, planning target volume; $D_{x\%}$, dose delivered to *x*% of the target volume; D_{max}, maximum dose.

Table 3
Acute and late adverse events of grade 3 or greater.

Toxicity	P-1 (*n* = 5)		P-2 (*n* = 5)				P-3 (*n* = 40)							
	Acute		Acute		Late		Acute				Late			
	Grade 3		Grade 3		Grade3		Grade 3		Grade 4		Grade 3		Grade 5	
	n	(%)	*n*	(%)	*n*	(%)	*n*	(%)	*n*	(%)	*n*	(%)	*n*	(%)
Hematologic														
Leukopenia	1	(20)	3	(60)			15	(38)	1					
Neutropenia	1	(20)	2	(40)			9	(23)	2					
Anemia			1	(20)										
Thrombocytopenia			1	(20)			2	(5)						
Gastrointestinal														
Nausea							2	(5)						
Vomiting							1	(3)						
Anorexia	1	(20)	1	(20)			3	(8)			1	(3)		
Epigastralgia	1	(20)					2	(5)						
Gastric ulcer					1	(20)					3	(8)	1	(3)
Miscellaneous														
Weight loss							3	(5)						
Fatigue	1	(20)					1	(3)			1	(3)		

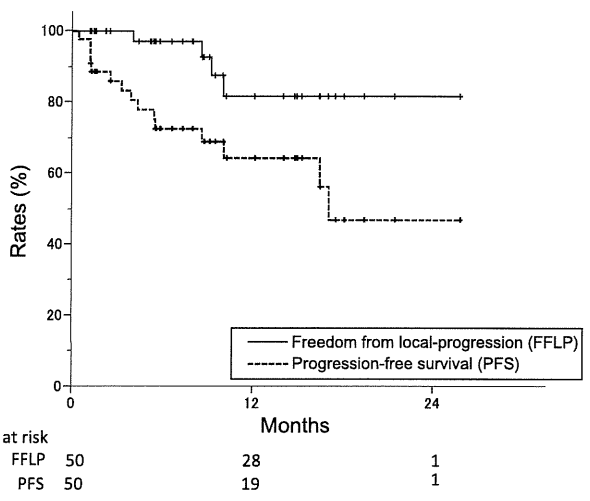

Fig. 2. The freedom from local-progression (solid line) and progression-free (dashed line) survival rates for all patients.

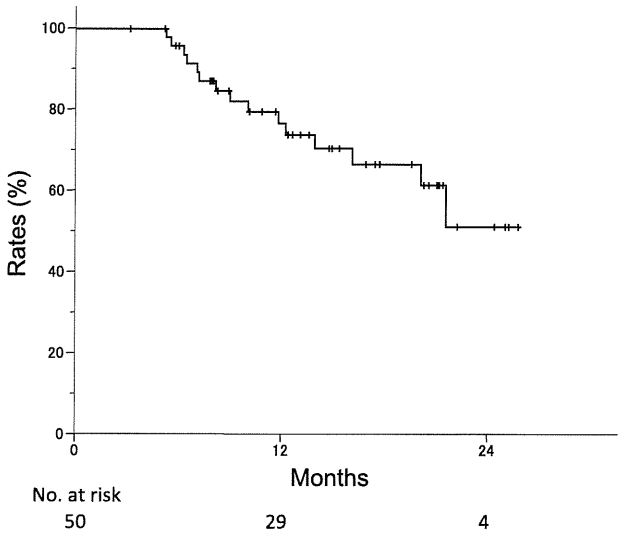

Fig. 3. The overall survival rate for all patients.

Society for Therapeutic Radiation and Oncology.

REFERENCES

1. Marbach JR, *et al* (1994) Management of radiation oncology patients with implanted cardiac pacemakers: report of AAPM Task Group No. 34. American Association of Physicists in Medicine. Med Phys **21**(1): 85–90.
2. Yoden E, *et al* (2007) A questionnaire survey on radiotherapy for patients with a pacemaker or an implantable cardioverter defibrillator. J Jpn Soc Ther Radiol Oncol **19**: 165–169. (in Japanese)
3. Bardy GH, *et al* (2005) Amiodarone or an implantable cardioverter-defibrillator for congestive heart failure. N Engl J Med **352**: 225–237.
4. Sanders GD, Hlatky MA and Owens DK (2005) Cost-effectiveness of implantable cardioverter-defibrillators. N Engl J Med **353**: 1471–1480.
5. Quertermous T, *et al* (1983) Pacemaker failure resulting from radiation damage. Radiology **148**: 257–258.
6. Lee RW, *et al* (1986) Runaway atrioventricular sequential pacemaker after radiation therapy. Am J Med **81**: 883–886.
7. Last A (1998) Radiotherapy in patients with cardiac pacemakers. Br J Radiol **71**: 4–10.
8. Marbach JR, *et al* (1978) The effects on cardiac pacemakers of ionizing radiation and electromagnetic interference from radiotherapy machines. Int J Radiat Oncol Biol Phys **4**: 1055–1058.
9. Marbach JR (1989) Recommended precautions in the management of radiation oncology patients with implanted pacemakers. ASTRO Newsletter **VIII**: 7–8.
10. Solan AN, *et al* (2004) Treatment of patients with cardiac pacemakers and implantable cardioverter-defibrillators during radiotherapy. Int J Radiat Oncol Biol Phys **59**(3): 897–904.
11. Gelblum DY and Amols H (2009) Implanted cardiac defibrillator care in radiation oncology patient population. Int J Radiat Oncol Biol Phys **73**(5): 1525–1531.
12. Sunder S, Symonds RP and Deehan C (2005) Radiotherapy to patients with artificial cardiac pacemakers. Cancer Treatment Reviews **31**: 474–486.
13. Jaeger M and Mirimanoff RO (1991) Hazards of radiotherapy in the presence of a cardiac pacemaker. Schweiz Rundsch Med Prax **80**(6): 109–111.
14. Howell RM, *et al* (2010) Methodology for determining doses to in-field, out-of-field and partially in-field organs for late effects studies in photon radiotherapy. Phys Med Biol **55**(23): 7009–7023.

Received on October 6, 2010
Revision received on February 17, 2011
Accepted on February 24, 2011
J-STAGE Advance Publication Date: April 14, 2011

Surface ligand assisted valence change in ceria nanocrystals

J. Zhang,[1] T. Naka,[1,2,*] S. Ohara,[1,3] K. Kaneko,[4,5] T. Trevethan,[6,7] A. Shluger,[6,7] and T. Adschiri[6]

[1]*Institute of Multidisciplinary Research for Advanced Materials, Tohoku University, Sendai 980-8577, Japan*

[2]*National Institute for Materials Science, Tsukuba, Ibaraki 305-0047, Japan*

[3]*Joining and Welding Research Institute, Osaka University, Ibaraki, Osaka 567-0047, Japan*

[4]*Department of Materials Science & Engineering, Kyushu University, Fukuoka 819-0395, Japan*

[5]*Core Research for Evolutional Science and Technology, Kyushu University, Fukuoka 819-0395, Japan*

[6]*WPI-Advanced Institute for Materials Research, Tohoku University, Sendai 980-8577, Japan*

[7]*Department of Physics and Astronomy, University College London, Gower Street, London WC1E 6BT, United Kingdom*

(Received 10 March 2011; published 6 July 2011)

In this report, we used x-ray absorption, electron energy-loss, and magnetic analyses to demonstrate the effect of modification of ceria ($CeO_{2-\delta}$) nanocrystals with a particle size $D = 3.5$–14 nm by oleic acid surface ligands. We observe a shift of the electronic state of the cerium ions from tetra to trivalent state as the surface density of the ligand molecules is increased. The valence state of cerium in the nanocrystal is strongly correlated with the number of ligand molecules bound to the surface of the ceria nanocrystals. One oxygen vacancy is stabilized by 5–6 ligand molecules bound on a $CeO_{2-\delta}$ nanocrystal.

DOI: 10.1103/PhysRevB.84.045411 PACS number(s): 61.46.Df, 81.07.Bc, 73.22.Dj, 71.30.+h

I. INTRODUCTION

Many of the physical and chemical properties of metal oxides, which are critical to a wide range of technological applications, can be controlled by inducing changes in the oxygen content of these compounds. For example, metal oxides with off-stoichiometric oxygen content have exhibited high-T_c superconductivity,[1] metal-insulator transitions,[2] and colossal magnetoresistance.[3] Moreover, changes in the oxygen content in such materials can promote and enhance catalytic activity[4,5] and ionic conduction.[6] Both static and dynamic changes in the valence of metal ions that occur at the interface between a metal oxide material and its environment can significantly influence its oxygen storage and transport capabilities, and this is particularly relevant in the case of nano-structured materials and nanoparticles with large surface areas. In this regard, cerium oxide (ceria) nanoparticles have received much attention owing to their remarkable ability to store and transport oxygen. The processes that underpin this ability are associated with a fast valence change in the compound, i.e., $Ce^{4+} \leftrightarrow Ce^{3+}$, and are often attributed to the creation of anionic vacancies, i.e., $CeO_2 \rightarrow CeO_{2-x} + (x/2)O_2$.

The synthesis of such metal oxide nanocrystals—with control over their size, shape, and surface features—is of fundamental technological interest because it is possible to tune both the size- and shape-dependent physical properties and also to prevent nanoparticle aggregation in a solvent. Recently, the organic-solution phase[7–9] and liquid–solid–solution phase synthetic-transfer routes[10] have been demonstrated to provide versatile pathways toward the controlled synthesis of metal oxide nanocrystals. In these methods organic surfactants can play a key role in controlling both the growth and stability of nanocrystals. Combining this concept and the properties of sub- and supercritical water (SCW) has lead to a novel approach for the synthesis of metal oxide nanocrystals. For example, SCW is chemically stable and processing with it is environmentally benign;[11] it acts as a unique medium to aid in the spontaneous nucleation and crystallization of metal oxide nanoparticles;[12] and by using organic ligand molecules that are miscible with SCW, crystal growth can be limited and agglomeration can be inhibited in favor of small, well-dispersed particles.[13,14] Additionally, since at the vicinity of the super critical point (374 °C, 22.1 MPa) where the properties of water change drastically, reaction equilibrium, adsorption equilibrium, and solubility also change remarkably; unique crystalline and surface bonding characteristics can be obtained. Under hydrothermal conditions in the presence of an organic surface modifier, a metallic source oxidizes and forms oxide nanocrystals since crystal growth (Ostwald ripening) is suppressed owing to the low solubility of oxides in super- or subcritical water. During crystallization the surface of the growing metal oxide interacts with and is modified by the organic-surface modifiers. This so-called *in-situ* surface modification is advantageous because it changes the surface nature of the nanocrystals from hydrophilic to hydrophobic and vice versa.[15,17]

In this paper we report that the tetra-to-trivalent transformation in ceria nanoparticles is facilitated by organic ligand molecule bonding on the exposed surfaces of the crystals and that this can occur at nanoparticle diameters significantly above $D = 3$ nm. It is well known that when the diameter of ceria nanoparticles decreases below approximately 3 nm, the average lattice constant of the crystal structure (a) begins to increase. Studies by Tsunekawa *et al.*,[18,19] Wu *et al.*,[20] Deshpande *et al.*,[21] and F. Zhang *et al.*[22] have indicated that trivalent cerium ions (Ce^{3+}) become dominant in the nanoparticles when the particle size decreases below this critical diameter, and that this change in valence is linked to the increase in lattice constant. However, large discrepancies in the precise relationship between the lattice constant and particle diameter between these different studies suggest that the cerium valence is not just a simple function of D. In fact, the cerium valence transformation may also depend on the nature of particle surfaces; i.e., the morphology of nanocrystals[18,19] and the termination of the crystal structure at exposed surfaces.[23]

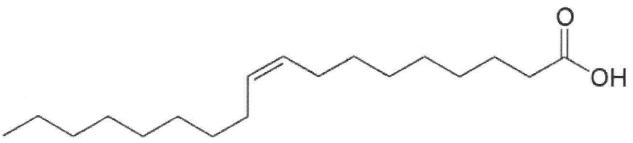

FIG. 1. Molecular structure of the oleic acid surface modifier.

Here we employed *in-situ* surface modification to synthesize ceria nanocrystals modified by oleic acid, which is a nontoxic fatty (hydrophobic) acid found in various vegetable and animal sources with a chain length of 2.2 nm (see Fig. 1). Quantitative analysis employing x-ray diffraction (XRD), electron energy-loss spectroscopy (EELS), Fourier transform infrared (FT-IR) spectra, and thermogravimetric–differential thermal analysis (TG-DTA) reveal that both the proportion of trivalent cerium (and the corresponding oxygen-vacancy concentration) and the lattice spacing are strongly correlated with the number of the ligand molecules adsorbed on the surfaces of the nanoparticles.

This approach to ceria nanoparticle synthesis demonstrates how both the oxygen content and the morphology of the ceria nanoparticles, both of which are critical to their reactivity and oxygen storage capacity, can be controlled through a careful choice of organic surface modifier. The plan of the remainder of the paper is as follows: in the next section we describe the methodology for sample preparation. Then in the following section we describe in detail the results of each of the analytical methods we employ (the details of which are included in as supplementary information). Finally we present a discussion of the results and conclusions.

II. EXPERIMENTAL METHODS

In a typical nanoparticle synthesis, the cerium oxide precursor was prepared by mixing 100 ml of 0.1 M $Ce(NO_3)_3$ solution with 100 ml of 0.3 M NaOH. After the reaction mixture had been stirred for approximately 6 h, the precursor was centrifuged and washed several times with distilled water. To synthesize nonmodified ceria nanocrystals, the 0.02-M precursor was transferred into a pressure-resistant SUS316 vessel (inner volume, 5 ml). The hydrothermal reaction was performed in the reactor for 10 min at a temperature range of 200–500 °C. A series of nonmodified nanocrystals with sizes of ~2 to ~15 nm was obtained by increasing the temperature of the reaction. To compare the influence of the surface ligands on the structural behavior of the ceria nanocrystals, an amount of oleic acid (in the range of 0.05–1 g) was also loaded into the vessel reactor. The hydrothermal reaction was then performed in the reactor at 400 °C for 10 min, as reported previously.[15] The nanocrystal size was managed by controlling the concentration of organic ligands in the reaction mixture.

XRD patterns were recorded on a RINT-2000 spectrometer (Rigaku, Tokyo, Japan) with Cu-Kα radiation. The samples were ground to fine powders before being subjected to XRD measurement. Transmission electron microscopy (TEM) images were obtained with a transmission electron microscope (JEM-1200EX, Japan) operated at 120 kV. High-resolution TEM (HRTEM) characterization was carried out using a Hitachi H-7100 electron microscope operating at 200 kV. The samples used for TEM and HRTEM measurements were dispersed in tetrahydrofuran (~0.1 weight%) before being transferred to carbon-coated copper grids. Thermogravimetric–differential thermal analysis (TG–DTA) was performed with a Thermo Plus TG8120 Rigaku instrument that was heated from room temperature to 100 °C at a rate of 10 °C min^{-1}. After maintaining a temperature of 100 °C for 30 min, the temperature was increased to 300 °C at a rate of 10 °C min^{-1} and maintained for 30 min again before heating to 800 °C at a rate of 10 °C min^{-1}. CaO was used as a reference compound for TG–DTA. FT-IR spectra were obtained on an FT-IR spectrometer (680 plus; FTIR JASCO Co.) at a resolution of 4 cm^{-1}. X-ray absorption near-edge structure (XANES) spectra at the Ce L_3-edge were carried out at ambient conditions in BL-7C (Photon Factory, KEK). To suppress unwanted harmonics, the angle between the monochromatic crystal faces was adjusted to mistune the incident beam by 30%. The incident and output-beam intensities were monitored and recorded using 30% helium-doped nitrogen gas and a nitrogen-flowing ionization chamber. The spectra were scanned in the range of 5.5–6.2 keV, which covers the L_3-edge absorption of cerium atoms. The samples were examined by field-emission TEM at 300 kV (TECNAI-30F with a postcolumn energy filter and a JEM-3200FSK with an in-column energy filter). The oxidation states were examined by EELS with energy resolution better than 0.9 eV. To measure the EELS edges, the beam width was maintained at approximately a few nanometers. Since electron beam irradiation might result in the loss of oxygen in ceria nonocrystals,[20] we determined an appropriate shorter irradiation time during EELS measurement. Magnetic measurements were carried out on a superconducting quantum interference device (SQUID) magnetometer (Quantum Design, MPMS) under a magnetic field up to 50 kOe in the temperature range between 4 and 100 K.

III. EXPERIMENTAL ANALYSIS

A. Crystallographic and morphological evolutions

Figure 2(a) shows XRD profiles for the synthesized products along with the simulated profiles for CeO_2 (with the fluorite structure) and the C-type $Ce_2O_{3-\delta}$.[24] All of the reflection peaks can be assigned to the cubic fluorite structure of ceria with respective lattice parameters. In the case of the unmodified nanocrystals, the crystal diameter was estimated from the line width by using Scherrer's equation and increases with increasing reaction temperature. As shown in Fig. 2(b), the lattice constant a is independent of nanoparticle diameter above 3.5 nm and corresponds to that of bulk stocheometric CeO_2 (a = 5.41 Å). However, in case of the modified nanocrystals, the lattice constant increases for nanocrystal sizes up to 7 nm, although the increment of a as a function of D for the modified nanocrystals is considerably smaller than those previously reported[18–21] but comparable with that obtained by Zhang *et al.*[22]

As stated previously, earlier studies[18–22] have indicated that the proportion of trivalent cerium significantly increases when the particle size decreases below a few nanometers. However, as shown in Fig. 2(b), here we observed significant differences in the relationship between the lattice constant

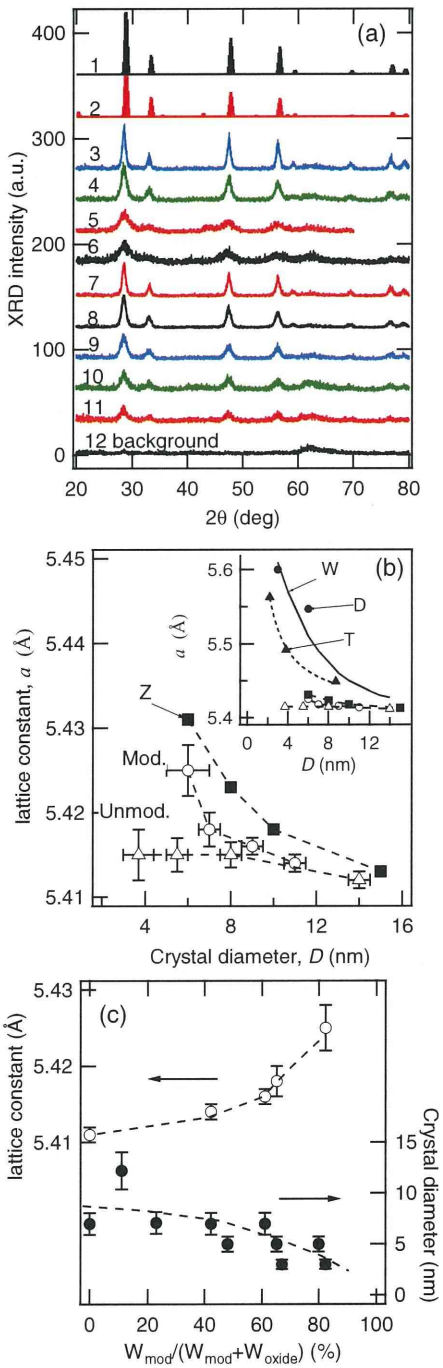

FIG. 2. (Color online) (a) XRD profiles 1 and 2 are simulated for CeO_2 (fluorite) and C-Ce_2O_3, respectively. The profiles 3–6 are of $CeO_{2-\delta}$ nanocrystals synthesized at 500, 400, 260, and 200 °C without the modifier, respectively. The profiles 7–11 are of $CeO_{2-\delta}$ nanocrystals synthesized with the molar ratio of the modifier to the metal precursor 4.5, 10.5, 18.9, 31.5, and 94.5, respectively. (b) Lattice constants as a function of particle size for ceria nanocrystals prepared by several research groups (denoted by T,[18,19] W,[20] D,[21] and Z[22]) and in the present study both with (Mod.) and without (Unmod.) organic modifiers. (c) Weight ratio of the modifier $R_{sm} = W_{mod}/(W_{mod} + W_{oxide})$ dependence on lattice constant and crystal size D.

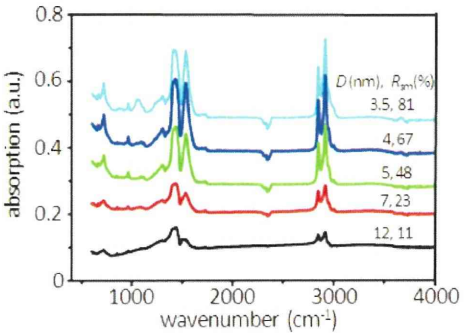

FIG. 3. (Color online) FT-IR spectra of the surface modified nanocrystals at various crystal diameters D and weight ratios R_{sm} for the surface modified ceria nanocrystals.

and D when we compared our present results with the results of these previously published studies. This suggests that the lattice expansion $\Delta a/a$, because of the valence transformation, depends not only on D but also on other quantities. As discussed in subsequent detail, we found that the cerium valence transformation (from Ce^{4+} to Ce^{3+}) depends strongly on both the particle's morphology and the surface modification by the oleic acid ligands.

B. FT-IR spectroscopy and Thermogravimetric–differential thermal analysis

The FT-IR spectra of ceria nanocrystals with varying degrees of oleic acid surface ligand coverage indicate that the chemical bonding between the surface ligands and the ceria surface is changed with increasing molecular coverage R_{sm} (Fig. 3). Here the coverage is defined according to the weight ratio of the modifier $R_{sm} = W_{mod}/(W_{mod} + W_{oxide})$ employed in the synthesis. Interestingly, Fig. 3 implies that the morphology of the ceria nanocrystals is transformed with increasing R_{sm} on the basis of the calculated binding structures described shortly. Spectral bands in the 2800–2960 cm^{-1} region are attributed to the C–H stretching mode of methyl and methylene groups (Fig. 3). It is worth noting that bands at 1532 and 1445 cm^{-1}, which are characteristic of the asymmetric (COO^-) and symmetric (COO^-) stretching modes, respectively, are present in the spectra of the ceria nanocrystals with surface ligands. The presence of these bands indicates that oleic acid is bound to the ceria nanocrystals as a form of carboxylate,[25–28] which can stabilize the Ce^{3+} state. With the decreasing of the nanocrystal size [Fig. 4(f)] and the change in morphology from cubic to truncated-cubic, as shown in Fig. 4(b)–4(e), the intensity ratio of (COO^-) at 1532 cm^{-1} to (COO^-) at 1445 cm^{-1} was enhanced, implying that the binding properties of the surface ligands on the ceria nanocrystals have changed.

The TG–DTA curves showed two distinct transitions between the room temperature and 800 °C for all samples tested [see typical results in Fig. 5(a)]. The first weight-loss peak, which occured around 290 °C, reveals that the oleate ligands dissociated from the surface of the ceria nanocrystals. The weight-loss peak at around 400 °C, corresponding to a chemical bonding between the organic ligands and the surface

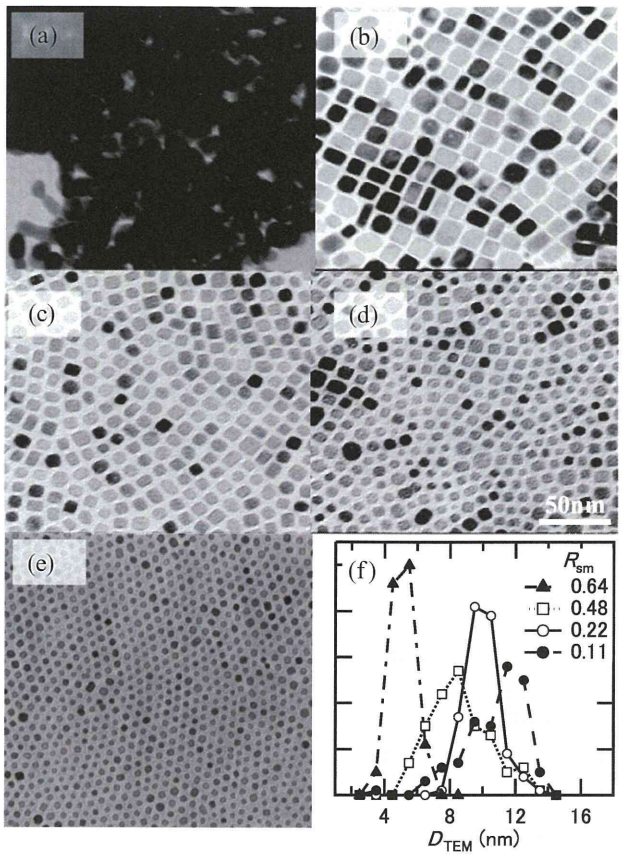

FIG. 4. TEM images of surface-modified ceria nanoparticles with surface ligand densities of $R_{sm} = 0$ (a), 0.11 (b), 0.22 (c), 0.48 (d), and 0.64 (e), respectively. Scale bar is 50 nm for all four panels. (f) Crystal size dispersion profiles for the respective R_{sm}. Lines between data points are the guides for eyes.

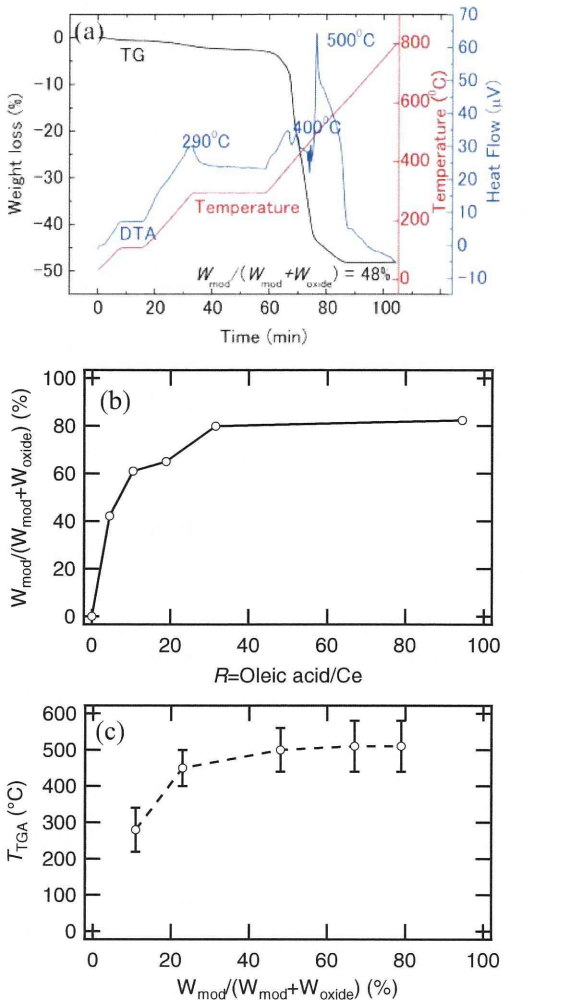

FIG. 5. (Color online) (a) TG–DTA curves (weight loss) for ceria nanocrystals with $R_{sm} = 48\%$. The curves were obtained at a heating rate of 10 °C/min. (b) Weight ratio of bonding organic molecule on ceria nanocrystals as a function of a molar ratio of surface ligand molecule and cerium ion in the precursor. (c) Dissociation point of the bonding organic molecules, T_{TGA}, as a function of weight ratio of the bonding organic molecules.

of the ceria nanocrystals,[29,30] was enhanced markedly with decreasing the ceria nanocrystal size. Remarkably these results indicate that the coverage of the ligands is increased with decreasing particle size, as shown in further discussion. This suggests that the morphology of the ceria nanocrystals depends strongly on the nature of the bonding interaction between the ceria surface and the organic ligands. Furthermore the binding state at the interface and the observed adsorption energy explain well the changing intensity ratio of the two peaks observed in the FT-IR spectra.[16]

C. Valence changes

The valence state of the ceria nanocrystals was evaluated by Ce L_3-edge XANES analysis, transmission electron microscopy with electron energy-loss spectroscopy (TEM-EELS), and magnetic susceptibility SQUID measurements under ambient conditions. XANES and TEM-EELS allow for direct observation of the cerium valence state. Figure 6(a) and (b) show Ce L_3-edge XANES spectra of the ceria nanoparticles. For comparison we also obtained Ce L_3-edge XANES spectra of the reference compound cerium(III) stearate ($Ce(C_{18}COO)_3$) and of bulk stoichiometric cerium(IV) oxide (CeO_2). The strongest peak (C) [assigned in Fig. 6(b)] observed for cerium(III) stearate is attributed to the dipole-allowed transition of Ce 2p to Ce $4f^15d$,[31–34] and this peak was assumed to correspond to trivalent cerium in the ceria nanocrystals. The cerium(IV) oxide XANES spectrum has a distinct double-peak structure (D,E) [assigned in Fig. 6(a)], and these peaks are attributed to the Ce 2p to 5d $L4f^1$ and 2p to $4f^0$ configurations, respectively, where L indicates a ligand (oxygen) hole. Using fitting procedures,[35,36] we obtained average valence transitions from the spectra of ceria nanocrystals of various sizes. As shown in Fig. 6(a), no significant change in the valence of cerium was observed for nonmodified ceria nanocrystals with particle sizes above 3 nm. In contrast when the surfaces of the nanocrystals were modified by organic ligands, their spectroscopic valence varied from +3.54 to +3.10 with decreasing particle size [Fig. 6(d)].

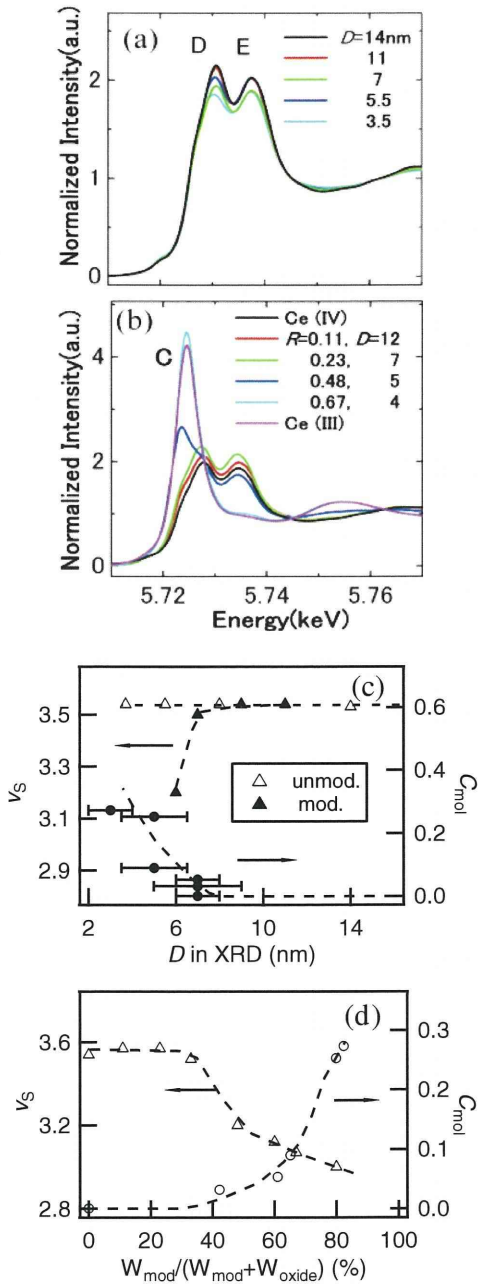

FIG. 6. (Color online) Ce L_3-edge XANES of ceria nanocrystals (a) without and (b) with surface ligands. Those of the reference compound cerium(III) stearate ($Ce(C_{18}COO)_3$) and of bulk cerium(IV) oxide (CeO_2) are also shown for comparison. The spectroscopic valence of cerium ions and Curie constant in the unit of emu/K mol estimated below 30 K (c) as a function of particle size and (d) as a function of weight ratio of the ligand molecule. Dashed lines are used to guide the eye.

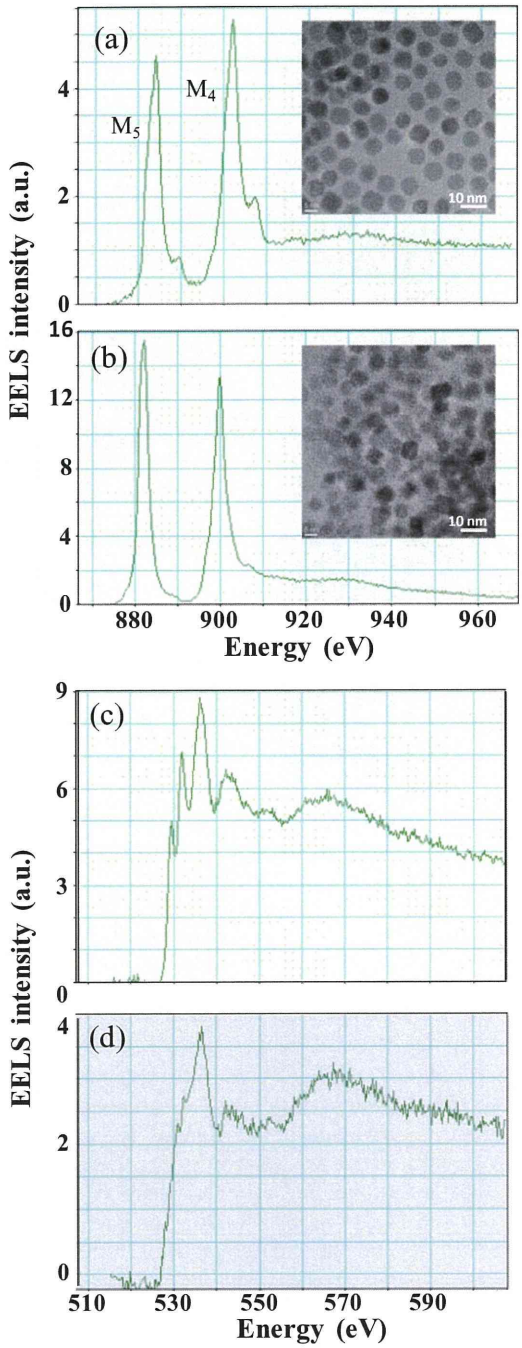

FIG. 7. (Color online) (a–d) TEM-EELS spectra of Ce $M_{4,5}$-edge with $R_{sm} = 0.33$ (a) and $R_{sm} = 0.67$ (b) and of O K-edges with $R_{sm} = 0.33$ (c) and $R_{sm} = 0.67$ (d). The TEM images from which these EELS spectra were obtained are shown in the insets of (a) and (b) for $R_{sm} = 0.33$ and 0.67, respectively.

To examine the valence state of the samples at the nanoscale, we also acquired TEM-EELS spectra [Fig. 7(a)–7(d)]. The TEM images from which the spectra were acquired are shown in the insets of Fig. 7(a) and 7(b). Within the Ce $M_{4,5}$-edge, two major peaks were observed for ceria nanocrystals with a surface ligand density of $R_{sm} = 0.33$ and 0.67, as shown in Fig. 7(a) and 7(b), respectively. The shape and position of these two peaks, referred to as M_5 and M_4, differed between the two ceria nanocrystal samples. For the sample with $R_{sm} = 0.67$, the positions of the peaks were shifted to a lower-energy region relative to those observed for the sample with $R_{sm} = 0.33$. Furthermore the M_5 and M_4 energy maxima were greater at $R_{sm} = 0.67$ than at $R_{sm} = 0.33$, and the intensity

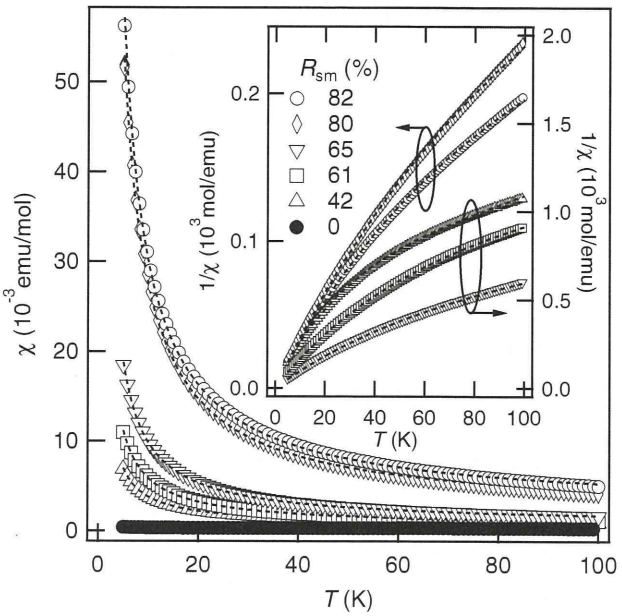

FIG. 8. (a) Temperature dependence of magnetic susceptibility of ceria nanocrystals with various weight ratios R_{sm}. Inset shows the reciprocal susceptibility at various weight ratios as a function of temperature. Dashed lines represent the fitted lines based on the crystal field scheme for the 4f-moment ($J = 5/2$) on Ce^{3+} in the cubic crystal ligand field with Γ_7 doublet (ground state) and Γ_8 quartet (excited state). The latter locates at Δ in energy above the ground state.

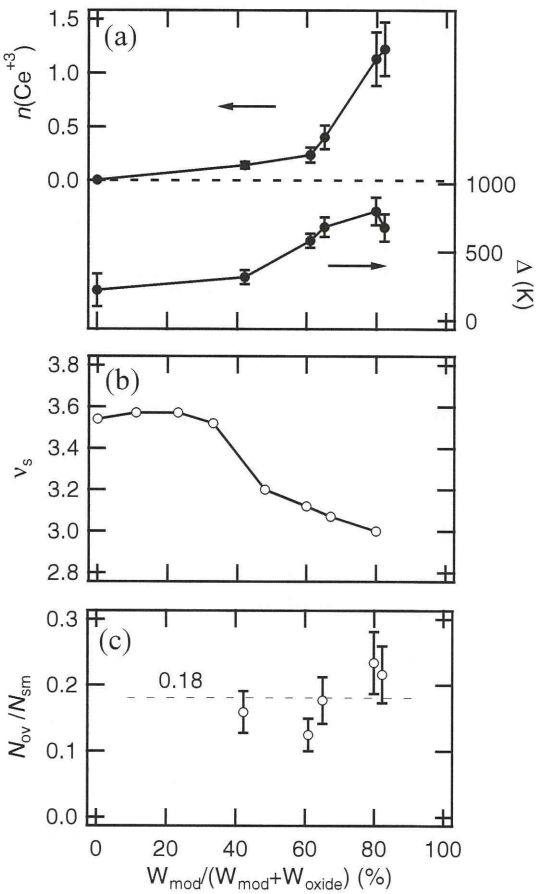

FIG. 9. The weight ratio's R_{sm} dependence of (a) the concentration of Ce^{3+}, $n(Ce^{3+})$ and the crystal field splitting Δ, (b) spectroscopic valence of cerium ion, and (c) ratio of number of oxygen vacancy N_{ov} to number of surface bonding molecule per crystal N_{sm}.

ratio for the two peaks was inverted such that M_5 was more intense for the $R_{sm} = 0.67$ sample relative to the $R_{sm} = 0.33$ sample. These changes are attributed to a typical transition from Ce^{4+} to Ce^{3+}, and such changes have been observed in $CeO_{2-\delta}$.[20,37] The O K-edges of samples with $R_{sm} = 0.33$ and 0.67 also exhibited different shapes, as shown in Fig. 7(c) and 7(d), respectively. For the sample with $R_{sm} = 0.33$, the edge had sharp characteristic peaks at 529.3, 532.0, and 536.2 eV, respectively. In contrast, for the sample with $R_{sm} = 0.67$, the O K-edge had rather broad peaks at 533.7 and 536.2 eV; this peak broadening is probably attributable to the lowest 4f orbital of cerium being filled, leaving no unoccupied part of the orbital that could be *p*-like and thus contribute to the O K-edge.

For the trivalent cerium ion, Ce^{3+}, a localized 4f moment is expected to be responsible for the ion's relatively larger magnetization in a magnetic field than that of Ce^{4+}, since Ce^{3+} has a ground state consisting of six-fold degenerate 4f states, $^2F_{5/2}$, and a total angular momentum of $J = 5/2$ while Ce^{+4} has $J = 0$. The temperature dependence of the magnetic susceptibility, $\chi(T)$, obeys Curie's law ($\chi \approx C/T$) below $T = 30$ K, as shown in Fig. 8, but deviates from the lower-temperature Curie law at higher temperatures, owing to thermal excitations of the excited crystal-field states. This characteristic temperature dependence of $\chi(T)$ results from a crystal-field effect. Since the Ce ion is located in the cubic-crystal field at the centre position of the face-centered cubic (FCC) unit cell, with oxygen atoms at the corners in the fluorite (CaF_2) structure, the six-fold degenerate 4f states of Ce^{3+} split into four-fold degenerate Γ_8 states and doubly degenerate Γ_7 states. On the other hand, in case of the crystal structure C-Ce_2O_3,[24] which is expected to be formed at $R_{sm} \sim 80\%$, all cerium ions are trivalent and located in the centers of O_6-octahedra. In this case, as is expected, the Γ_7 state is the ground state while for the Ce^{3+} ion located at the body center of FCC unit cell the Γ_8 state is the ground state. A possible explanation for this is that the coordination number of Ce ion is reduced with increasing R_{sm}, which is consistent with density functional theory (DFT) calculations[38] that show that the Ce^{3+} ion locates along with the oxygen vacancy. Therefore we can assume the octahedral-cubic crystal field, that is, the Γ_7 doublet is the ground state and the Γ_8 quartet locates at Δ in energy above the Γ_7 level. In fact, as shown in Fig. 8, the susceptibility-temperature data can be fitted well with this assumption. Figure 9(a) shows the concentration of Ce^{3+} ions, $n(Ce^{3+})$, and Δ as a function of R_{sm}. Notably, the gradient of $n(Ce^{3+})$ with respect to R_{sm} changes steeply, with the corresponding changes in XANES spectra occurring as shown in Fig. 9(b). It is recently indicated, similar to our findings, that oxygen vacancy of $CeO_{2-\delta}$ nanoparticles with $D = 2.7$–3.5 nm

produced by thermal decomposition method is stabilized with surfactant.[39] Surprisingly, the vacancy in $CeO_{2-\delta}$ nanocrystal seems to bring about a small ferromagnetic moment (0.01–0.12 emu/g) at room temperature. In contrast, it should be emphasized that this room-temperature ferromagnetism is hardly detectable in the surface-modified nanoparticle samples examined in this study.

Assuming that the valence change of cerium is predominantly attributable to the formation of oxygen vacancies in $CeO_{2-\delta}$ nanocrystals,[38–41] the previous analysis suggests that these vacancies are created and/or stabilized by the bonding of the oleic acid molecules to the surface. Around $R_{sm} \sim 80\%$ the cerium ion is trivalent. Therefore, the valence of cerium is related to the number of ligand molecules bound on the surface of the nanoparticle. In fact, as shown in Fig. 9(c), the ratio of the number of oxygen vacancies to the number of ligand molecules (per crystal), N_{ov}/N_{sm} is approximately 0.18. Although it is not obvious whether the ratio is a constant of R_{sm}, this suggests one oxygen vacancy is stabilized by approximately 5–6 oleic acid molecules adsorbed on the nanocrystal surface.

IV. DISCUSSION AND CONCLUSION

The detailed analysis presented in this paper has demonstrated that nonmodified ceria nanocrystals showed no substantial valence change under ambient conditions with particle sizes greater than $D \sim 3$ nm, whereas nanocrystals with surfaces modified with oleic acid exhibited a strong size and surface modification-dependent variation in valence states below diameters of 7 nm [Fig. 6(c) and (d)]. These experimental results indicate that the modification of the surface with oleic acid ligands can induce a valence transition from Ce^{+4} to Ce^{+3} in the nanocrystals. This provides important insights for understanding the electronic and structural changes that result from interactions between surface ligands and the electronic states of metal oxide nanocrystals.

These findings imply that the static valence transformation from Ce^{4+} to Ce^{3+} is dependent strongly on both the crystal size and the surface coverage of organic ligands. One possible explanation for this is that neutral oxygen vacancies (the formation of which results in the Ce ion valence change) are stabilized by ligand molecules binding to the nanoparticle surface. An alternative explanation is that the valence change is caused by changes in the coordination of surface ions, which is dependent on the crystal shape and structure of the surface (which may be modified by the molecular adsorbates).

As discussed previously, there is a large discrepancy in $a(D)$ among previous studies[18,20,22,41] as well as between those studies and our present study [Fig. 2(b)]. This discrepancy indicates that, as the crystal size decreases, $\Delta a/a$ is a function not only of valence state but also of the surface structure of the nanocrystals, namely, the surface morphology (exposed crystallographic surfaces) and the extent of surface modification by organic molecules. This may be attributable to different changes in the crystal structure caused by the formation of oxygen vacancies on different crystallographic surfaces. If the formation of vacancies on either the (111) or (001) facets resulted in a greater or smaller change in average interatomic distances, the lattice parameter would depend on the morphology, which is suggested by DFT simulations.[40,42] In addition, changes in surface structure may occur because of the interaction with adsorbed molecules, which would result in the lattice parameter being dependent on both the coverage and morphology. DFT studies have demonstrated that the average interatomic distances in small, unmodified ceria nanoparticles are most significantly affected by the creation of oxygen vacancies,[42] however, this was only considering octohedral particles with (111) exposed surfaces.

Using XRD and high-resolution TEM, F. Zhang *et al.*[22] observed the exposed (111) surface in most of their ceria nanoparticles, whereas Wu *et al.*[20] observed their ceria nanoparticles to be spherical. Tsunekawa *et al.*[18,19] have indicated that their ceria nanoparticles are a mixture of octahedral and spherical particles surrounded by a (111) plane and different crystallographic surfaces, respectively.[41,43]

Atomistic simulations have demonstrated that the morphology of unmodified ceria nanoparticles are truncated octohedra[44] consisting of both (111) and (001) terminating surfaces, with the (111) surface dominating because of its lower surface energy.[45] The energy required to form oxygen-atom vacancies on both of these surfaces is relatively high: for the (111) surface the vacancy-formation energy is calculated (with DFT and with respect to half an O_2 molecule) as 3.3 eV[40] and on the (001) surface as 2.9 eV.[40] However, recent calculations have demonstrated that the oxygen vacancy formation at low-coordinated oxygen sites at corners and edges of truncated octohedral nanoparticles requires much lower energies (as low as 0.58 eV).[46] The proportion of low-coordinated oxygen atoms increases as the nanoparticle size decreases, and therefore the valence transformation is greatly facilitated. DFT calculations of the formation of oxygen vacancies at both (111) and (001) facets have demonstrated that the extraction of a neutral oxygen from the surface (and subsurface) results in the reduction of two neighboring Ce(IV) atoms to Ce(III), creating a new state in the ceria band gap below the unoccupied Ce 4f states, which is consistent with these results.[40,47]

DFT calculations have also demonstrated how carboxylic acids can stabilize oxygen vacancies on ceria surfaces. In Gordon *et al.*[48] the adsorption energy of formic acid on the (111) surface of ceria is calculated to be 1.07 eV and the acid is deprotonated on the surface (the molecule binds as a carboxylate, as suggested by the IR spectroscopy in this study). The binding energy of the molecule to a single oxygen vacancy, however, increases to 3.95 eV, which is larger than the vacancy formation energies on both the (111) and (001) surfaces. These calculations suggest that carboxylic acid molecules can facilitate the formation of oxygen vacancies at ceria surfaces [particularly at the low-coordinated sites and on the (001) surface], which can explain the overall valence change observed in this study as the coverage of the molecules is increased. However, further calculations are required to fully understand how carboxylic groups interact with low-coordinated vacancies and vacancies in the (001) surface, which is key to the valence transformation and its relationship to the coverage of the molecules. Another key component to understanding the ratio between the number

of surface ligands and the number of oxygen vacancies is the interaction between the oleic acid molecules, which will contribute to surface energies and affect both the relative coverage on different surfaces and the morphology of the particles.

After removing surface bonding molecules (hexanoic acid) by treating the samples in air at 150 °C, the morphology of ceria nanocrystals does not change and the crystal structure is stable.[49] Consequently, the crystals possess a high proportion of highly activated crystallographic surfaces, such as (001) planes, realized by using the *in-situ* surface modification. These particles then reversibly show an unexpectedly high oxygen storage capacity performance even at extremely low temperatures.[49]

ACKNOWLEDGMENTS

We would like to express our appreciation to Dr. S. Tsunekawa in IMR, and Drs. H. Isago and H. Suzuki in NIMS for valuable discussions. This work was partially supported by the Grant-in-Aid for Scientific Research, KAKENHI, (17206078, 19310063, and 20226015).

*naka.takashi@nims.go.jp

[1] E. Takayama-Muromachi, Y. Uchida, M. Ishii, T. Tanaka, and K. Kato, Jpn. J. Appl. Phys. Part 2 **26**, L1156 (1987).
[2] F. Iga and Y. Nishihara, J. Phys. Soc. Jpn. **61**, 1867 (1992).
[3] É. L. Nagaev, in *Colossal Magnetoresistance and Phase Separation in Magnetic Semiconductors* (Imperial College Press, London, 2002), Ch. 7, p. 297.
[4] A. Trovarelli, Catal. Rev. Sci. Eng. **38**, 439 (1996).
[5] A. J. Zarur and J. Y. Ying, Nature **403**, 65 (2000).
[6] S. D. Park, J. M. Vohs, and R. J. Gorte, Nature **404**, 265 (2000).
[7] T. Hyeon, S. S. Lee, J. Park, Y. Chung, and H. B. Na, J. Am. Chem. Soc. **123**, 2798 (2001).
[8] J. Rockenberger, E. C. Scher, and A. P. Alivisatos, J. Am. Chem. Soc. **121**, 11595 (1999).
[9] J. Park, K. An, Y. Hwang, J. G. Park, H. J. Noh, J. Y. Kim, J. H. Park, N. M. Hwang, and T. Hyeon, Nat. Mater. **3**, 891 (2004).
[10] X. Wang, J. Zhuang, Q. Peng, and Y. D. Li, Nature **437**, 121 (2005).
[11] H. Weingartner and E. U. Franck, Angew. Chem. Int. Ed. **44**, 2672 (2005).
[12] T. Adschiri, Y. Hakuta, and K. Arai, Ind. Eng. Chem. Res. **39**, 4901 (2000).
[13] K. J. Ziegler, R. C. Doty, K. P. Johnston, and B. A. Korgel, J. Am. Chem. Soc. **123**, 7797 (2001).
[14] P. S. Shah, T. Hanrath, K. P. Johnston, and B. A. Korgel, J. Phys. Chem. B **108**, 9574 (2004).
[15] J. Zhang, S. Ohara, M. Umetsu, T. Naka, Y. Hatakeyama, and T. Adschiri, Adv. Mater. **19**, 203 (2007).
[16] M. Taguchi, S. Takami, T. Naka, and T. Adschiri, Crystal Growth & Design, **9**, 5297 (2009).
[17] T. Arita, Y. Ueda, K. Minami, T. Naka, and T. Adschiri, Ind. Eng. Chem. Res. **49**, 1947 (2010).
[18] S. Tsunekawa, T. Fukuda, and A. Kasuya, J. Appl. Phys. **87**, 1318 (2000).
[19] S. Tsunekawa, K. Ishikawa, Z. Q. Li, Y. Kawazoe, and A. Kasuya, Phys. Rev. Lett. **85**, 3440 (2000).
[20] L. J. Wu, H. J. Wiesmann, A. R. Moodenbaugh, R. F. Klie, Y. M. Zhu, D. O. Welch, and M. Suenaga, Phys. Rev. B **69**, 125415 (2004).
[21] S. Deshpande, S. Patil, S. V. N. T. Kuchibhatla, and S. Seal, Appl. Phys. Lett. **87**, 133113 (2005).
[22] F. Zhang, S.-W. Chan, J. E. Spanier, E. Apak, Q. Jin, R. D. Robinson, and I. P. Herman, Appl. Phys. Lett. **80**, 127 (2002).
[23] K. Kaneko, K. Inoke, B. Freitag, A. B. Hungria, P. A. Midgley, T. W. Hansen, J. Zhang, S. Ohara, and T. Adschiri, Nano. Lett. **7**, 421 (2007).
[24] E. A. Kummerle and G. Heger, Journal of Solid State Chemistry **147**, 485 (1999).
[25] V. Bolis, G. Magnacca, G. Cerrato, and C. Morterra, Therm. Acta. **379**, 147 (2001).
[26] C. Binet and M. Daturi, Catal. Today. **70**, 155 (2001).
[27] Y. G. Aronoff, B. Chen, G. Lu, C. Seto, J. Schwartz, and S. L. Bernasek, J. Am. Chem. Soc. **119**, 259 (1997).
[28] J. E. Tackett, Appl. Spectrosc. **43**, 483 (1989).
[29] Y. Sahoo, H. Pizem, T. Fried, D. Golodnitsky, L. Burstein, C. N. Sukenik, and G. Markovich, Langmuir **17**, 7907 (2001).
[30] L. F. Shen, P. E. Laibinis, and T. A. Hatton, Langmuir **15**, 447 (1999).
[31] G. Kaindl, G. Schmiester, and E. V. Sampathkurmaran, Phys. Rev. BI **38**, 10174 (1988).
[32] A. V. Soldatov, T. S. Ivanchenko, S. D. Longa, A. Kotani, Y. Iwamoto, and A. Bianconi, Phys. Rev. B **50**, 5074 (1994).
[33] L. Douillard, M. Gautier, N. Thromat, and J. P. Duraud, Nucl. Instr. Meth. Phys. Res. B **97**, 133 (1995).
[34] T. W. Capehart, R. K. Mishra, and J. F. Herbst, J. Appl. Phys. **72**, 676 (1992).
[35] P. Nachimuthu, W. Shih, R. Liu, L. Jang, and J. Chen, J. Solid State Chem. **149**, 408 (2000).
[36] D. Bazin, D. Sayers, J. J. Rehr, and C. Mottet, J. Phys. Chem B **101**, 5332 (1997).
[37] L. A. J. Garvie and P. R. Buseck, J. Phys. Chem. Sol. **60**, 1943 (1999).
[38] N. V. Skorodumova, S. I. Simak, B. I. Lundqvist, I. A. Abrikosov, and B. Johansson, Phys. Rev. Lett. **89**, 166601 (2002).
[39] S.-Y. Chen, Y.-H. Lu, T.-W. Huang, D.-C. Yan, and C.-L. Dong, J. Phys. Chem. C **114**, 19576 (2010).
[40] M. Nolan, S. C. Parker, and G. W. Watson, Surf. Sci. **595**, 223 (2005).
[41] S. Tsunekawa, S. Ito, and Y. Kawazoe, Appl. Phys. Lett. **85**, 3845 (2004).
[42] C. Loschen, A. Migani, S.T. Bromley, F. Illas, and K. M. Neyman, Phys. Chem. Chem. Phys. **10**, 5730 (2008).
[43] S. Tsunekawa, R. Sivamohan, S. Ito, A. Kasuya, and T. Fukuda, Nanostructured Materials **11**, 141 (1999).
[44] T. Sayle, S. C. Parker, and D. C. Sayle, Chem. Commum. **21**, 2438 (2004).

[45]M. Nolan, S. Grigoleit, D. C. Sayle, S. C. Parker, and G. W. Watson, Surf. Sci. **576**, 217 (2004).

[46]A. Migani, G. N. Vayssilov, S. T. Bromley, F. Illas, and K. M. Neyman, J. Materials Chem. **20**, 10535 (2010).

[47]M. V. Ganduglia-Pirovano, J. L. F. Da Silva, and J. Sauer, Phys. Rev. Lett. **102**, 026101 (2009).

[48]W. O. Gordon, Y. Xu, D. R. Mullins, and S. H. Overbury, Phys. Chem. Chem. Phys. **11**, 11171 (2009).

[49]J. Zhang, H. Kumagai, K. Yamamura, S. Ohara, S. Takami, A. Morikawa, H. Shinjoh, K. Kaneko, T. Adschiri, and A. Suda, Nano. Lett. **11**, 361 (2011).

Journal of Materials Chemistry

View Online
Dynamic Article Links

Cite this: J. Mater. Chem., 2011, 21, 12008

www.rsc.org/materials

PAPER

Ordered deposition of Pd nanoparticles on sodium dodecyl sulfate-functionalized single-walled carbon nanotubes

Zhenquan Tan,* Hiroya Abe and Satoshi Ohara

Received 10th April 2011, Accepted 24th May 2011
DOI: 10.1039/c1jm11514f

We report here a novel chemical solution method to site-selectively deposit and arrange palladium (Pd) nanoparticles (NPs) on single-walled carbon nanotubes (SWCNTs). Sodium dodecyl sulfate (SDS) formed supramolecular self-assemblies on the SWCNTs. The SDS then acted as adsorption sites for Pd(II) ions. Pd(II) was reduced to Pd NPs by photo-reduction, and the NPs formed helices with different helix angles on the surface of the SWCNTs. The pitch of the Pd NPs helix was 4.5 nm. The parameters of the Pd NPs helix (pitch, angle, and chirality) were determined by the supramolecular self-assembly of SDS on the SWCNTs. Increasing the concentration of Pd(II) ions resulted in high-density deposition of Pd NPs on the SDS-functionalized SWCNTs.

Introduction

Carbon nanotubes (CNTs) have attracted significant research interest in recent years because of their unique one-dimensional structure and potential applications in many fields.[1–4] CNTs are regarded as ideal one-dimensional templates for deposition of metal nanoparticles (NPs).[5] This provides a potential route for simple synthesis of various heterogeneous nanostructures, which could be applied as high-performance catalysts, fuel cells and (bio)chemical sensors.[6–11] Numerous methods have been developed to fabricate CNTs based metal nanocomposites, including surface functionalization of CNTs,[12–16] self-assembly,[17,18] electrochemistry,[19,20] supercritical fluid synthesis[21] and plasma treatment.[22] However, the design and control of ordered heterogeneous nanostructures on the surfaces of CNTs is still a challenge. Many research groups have focused on the ordered self-assembly behavior of polymers and/or other organic macromolecules on the surface of CNTs.[23–33] For example, Li *et al.* reported the formation of alternating periodic patterns of copolymers on the surface of CNTs.[30–32] Based on this approach, they successfully constructed heterogeneous nanostructures on one-dimensional CNTs by immobilization of gold NPs on the block copolymer/CNT hybrid.[33]

Recently, surfactant-functionalized CNTs have been considered for synthesis of ordered heterogeneous nanostructures. Surfactants are advantageous because they disperse CNTs in water and alter the physical and chemical properties of the CNT's surface.[34,35] Sodium dodecyl sulfate (SDS) is the most common surfactant used in this area.[36,37] The alkyl group of SDS adsorbs on the CNTs by hydrophobic interaction, and the hydrophilic tail orientates toward the aqueous phase. Because CNTs are cylindrical graphene sheets, the SDS self-assembles into a half-cylinder structure on the surface of the CNTs.[38] The supramolecular nanostructure of SDS-functionalized CNTs makes them an ideal template to fabricate designed heterogeneous nanostructures on CNTs. Recently, we reported site-selective deposition of Pd NPs on single-walled carbon nanotubes (SWCNTs) using the supramolecular self-assembly of SDS as a soft template.[39] The deposited Pd NPs formed ordered arrangements around the SDS-functionalized SWCNTs. This SDS template approach has four obvious advantages over other methods. First, SDS is highly effective at dispersing SWCNTs in water, which is very important for solution chemistry of SWCNTs. Second, SDS can self-assemble into a supramolecular structure wrapped around the SWCNTs, which is an ideal soft template for arrangement of NPs or quantum dots (QDs) on SWCNTs. Third, SDS is a small molecule and bonds to SWCNTs by van der Waals interactions. This makes it easy to remove SDS from SWCNTs by washing with alcohol and filtration. Finally, SDS is an environmentally friendly reagent, easy to obtain, and cheap. Consequently, SDS is practical for application as a template in the synthesis of CNTs-based nanostructures.

In this article, we discuss the fabrication and control of ordered Pd nanostructures on SDS-functionalized SWCNTs. Pd is a high-performance metal that has been extensively studied for possible applications in fuel cells, high-performance catalysts and hydrogen storage.[40–42] Consequently, high-density deposition of Pd NPs on SWCNTs is complementary to the potential applications of SWCNTs. Because the electrostatic interaction between the negatively charged functional group of SDS and positively charged metal ion is non-selective, this facile approach could be used to site-selectively deposit other metal NPs on SDS-functionalized SWCNTs.

Joining and Welding Research Institute, Osaka University, Mihogaoka 11-1, Ibaraki, Osaka, Japan. E-mail: zq-tan@jwri.osaka-u.ac.jp; Fax: +81 668 79 4370; Tel: +81 668 79 4370

Experiment

Materials

High purity SWCNTs materials were purchased from Carbon Nanotechnologies Inc. (Houston, TX) and used without further purification. SDS (99.0% purity) was purchased from Kishida Chemical (Osaka, Japan). Palladium chloride ($PdCl_2$, 99.0% purity) and silver nitrate ($AgNO_3$, 99.8% purity) were obtained from Wako Pure Chemical Industries, Ltd. (Wako, Japan) and Kanto Chemical Co., Inc. (Tokyo, Japan), respectively. All of the reagents were used as received. Distilled water (resistivity > 18 mΩ) for use in this study was prepared by an ultrapure water purification system (Sartorius AG, Germany).

Preparation

The site-selective synthesis of Pd NPs templated by supramolecular self-assembly of SDS-functionalized SWCNTs is illustrated in Scheme 1. An aqueous solution (10 mL) containing mass fractions of 0.5% SDS and 0.05% SWCNTs (5 mg) was mixed for 8 h in a ball-mill as described previously.[43,44] This separated the large bundles of SWCNTs into individual nanotubes and/or small bundles, and dispersed them in the SDS aqueous solution. SDS molecules were adsorbed onto the surfaces of SWCNTs and formed helical supramolecular self-assemblies oriented perpendicular to the CNT axis.[38] A 2 mL aqueous solution of $PdCl_2$ (20 mM) was added to the SDS-functionalized SWCNTs solution. The Pd(II) cations selectively absorbed onto the walls of SWCNTs where the SDS molecules were located because of electrostatic interaction between the Pd(II) cation and the anionic sulfate groups in SDS. The mixed solution was then irradiated for 60 min by a UV lamp ($\lambda = 254$ nm). This resulted in photoreduction of the Pd(II) to Pd NPs that were site-selectively formed in an ordered manner on the surface of SWCNTs. This synthesis used the supramolecular self-assembly of SDS as a soft patterning template.

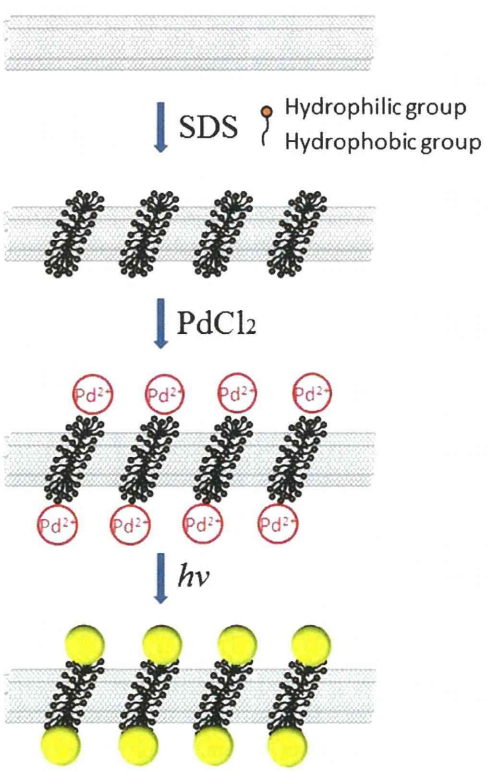

Scheme 1 Arrangement of Pd NPs on the SDS-functionalized SWCNTs.

Characterization

A dispersion of each sample was dropped and filtered onto a filter membrane, dried in air, and then examined by field-emission scanning electron microscope (FE-SEM, Hitachi SU-70, Japan). The produced nanostructures were also deposited onto a carbon-coated Cu grid, dried, and observed by transmission electron microscope (TEM, JEM-2100F, JEOL, Japan). Atomic force microscope (AFM) investigations of the samples were carried out on a NanoNavi S-image SPM system (SII, Japan) using fresh mica as the substrate. The absorption properties of the resulting products were evaluated in the solution state using a visible-near infrared (Vis-NIR) scanning spectrophotometer (UV-3100PC, Shimadzu, Japan). Powder samples were analyzed by X-ray diffraction (XRD) spectroscopy (JDX-3530M, JEOL, Japan). Raman spectrum was performed using a four-wavelength Raman spectrometer (LabRAM ARAMIS, Horiba, Japan), recorded at room temperature by using 532 nm (2.33 eV) laser excitation. The Pd–SWCNT nanostructures were also characterized by diffuse reflectance Fourier-transform infrared spectroscopy (FTIR, IRPrestige-21, Shimadzu, Japan) in KBr matrix.

Results and discussions

SDS-functionalized SWCNTs

The SWCNTs were originally in large bundles with an average diameter of 50 nm because of van der Waals interactions

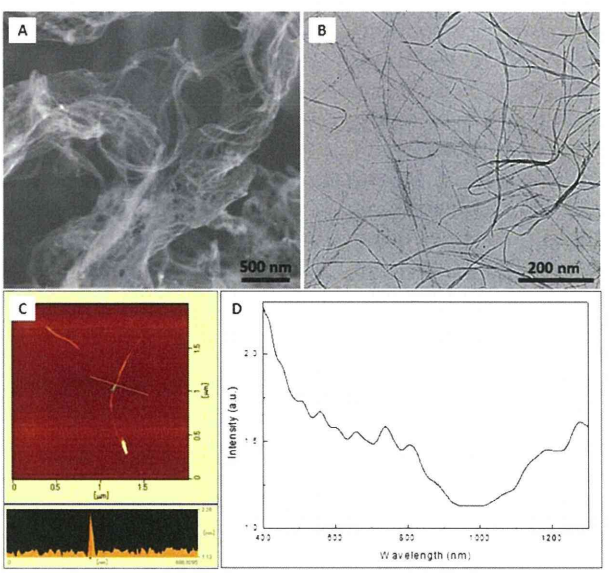

Fig. 1 SEM image of the original SWCNTs (A), and TEM image (B), AFM images (C) and absorption spectrum (D) of the dispersed SWCNTs after addition of SDS.

(Fig. 1A). When SDS was added it absorbed onto the surface of the CNTs *via* hydrophobic interaction between the hydrophobic chain of SDS and the sidewalls of the CNTs.[37,38] This intercalation of the surfactant molecules between CNTs effectively separated the bundled CNTs into much smaller bundles and/or individual CNTs, which is illustrated in a typical TEM photograph of the dispersed SWCNTs (Fig. 1B). The diameter from the cross-sectional profile of the AFM image (Fig. 1C) was consistent with that of SWCNTs, which suggests separation of the large SWCNTs bundles was successful. Fig. 1D shows a typical Vis-NIR absorption spectrum of the SDS-dispersed SWCNTs in water. Numerous absorption peaks originating from the van Hove maxima electronic density of the quasi one-dimensionality of the SWCNTs[45] appeared from 500–1300 nm, which is another indicator of the presence of single tubes and small bundles of dispersed SWCNTs.[43]

The SDS molecules were not homogeneously absorbed over the entire surface of SWCNTs, but formed an ordered supramolecular self-assembly on the SWCNTs.[39] Fig. 2A shows a high resolution TEM photograph of the dispersed SWCNTs and periodic ordered SDS supramolecular self-assemblies on their surfaces. A magnification of the SDS-functionalized SWCNTs is shown in Fig. 2B. The ordered SDS nanostructures had various helix angles, which depended on the diameter of the CNTs. The pitch of the SDS helix was 4.5 ± 0.5 nm, which agrees with previous research.[38]

Pd NPs arranged on the SWCNTs

Because SDS is an anionic surfactant, metal cations may be electrostatically absorbed onto the surface of SDS-functionalized SWCNTs. The metal ions can then be reduced to metal NPs by a photoreduction reaction as illustrated in Scheme 2. The ordered supramolecular self-assembly of SDS on the surface of the SWCNTs provides a suitable soft template for construction of ordered heterogeneous nanostructures by deposition of the NPs on the one-dimensional SWCNTs. Fig. 3A shows a typical TEM photograph of sample A. The high-resolution TEM photograph (Fig. 3B) showed the Pd NPs were clearly arranged in ordered structures on the surface of the SWCNTs. The Pd NPs were 2.5 ± 0.5 nm in diameter. The pitch of the NP helix was the same as that of the SDS helix at 4.5 ± 0.5 nm, which indicates that the Pd NPs were selectively deposited onto the SDS-functionalized SWCNTs at the location of the SDS supramolecular self-assemblies.

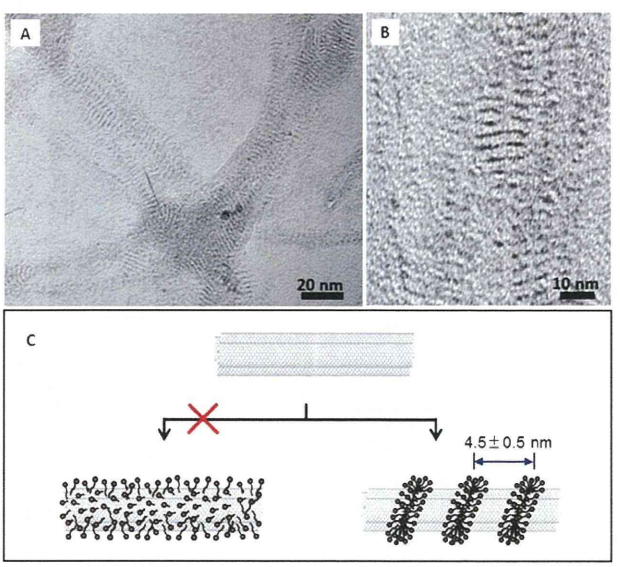

Fig. 2 High-resolution TEM images of SDS-functionalized SWCNTs (A and B) and a scheme (C) for the formation of the helical supramolecular self-assembly of SDS on the surface of the SWCNTs.

It has previously been reported that the helical angle of supramolecular self-assembled SDS molecules depends on the diameter of the SWCNTs.[38] We observed different helical arrangements of Pd NPs on the SDS-functionalized SWCNTs (Fig. 4A–C). These included right-handed helices with helix angles of −16° (Fig. 4A) and −6° (Fig. 4B), and a left-handed helix with a helix angle of 5° (Fig. 4C). Interestingly, Pd NPs arrangements with both right- (−24°) and left-handed (3°) helices were also observed on an individual bundle of SWCNTs (Fig. 4D). This indicates that the SDS supramolecular self-assembly wrapped around this bundle of SWCNTs included both types of helices. A dark field STEM image (Fig. 4E) of the Pd NPs wrapped around the SWCNTs also clearly showed the ordered nanostructures of the Pd NPs.

High density deposition of Pd NPs

Increasing the concentration of the $PdCl_2$ from 20 mM to 50 mM resulted in a much higher density of site-selectively deposited Pd NPs (Fig. 5A). The average diameter of the Pd NPs also slightly increased to 3.5 ± 0.5 nm when the concentration of $PdCl_2$ was increased. The helical structures observed on this sample were left-handed with a helix angle of 18° (Fig. 5B), and right-handed with helix angles of −45° (Fig. 5C) and −39° (Fig. 5D). Disorder of the Pd NPs increased when larger numbers of Pd NPs were deposited onto the SDS functionalized SWCNTs. This may occur because the reduction rate of Pd NPs was higher than the equilibrium rate of Pd absorbed onto the SDS molecules. The disordered Pd NPs made it difficult to distinguish the ordered arrangements of Pd NPs wrapped around the SWCNTs. Because Pd is a high-performance metal that has been widely studied for possible applications in many fields,[40–42] its deposition on the SWCNTs is expected to enhance the catalytic performance of the SWCNT–Pd heterogeneous nanocomposites.

Optical and other properties

UV-Vis absorption spectroscopy was used to characterize the photoreduction reaction of Pd(II) ions on the SDS-functionalized SWCNTs (Fig. 6A). Spectra of the $PdCl_2$ solutions on their own showed strong absorption peaks at 420 nm, which originated from the *d–d* electronic transition of the Pd(II) ions.[46] In contrast, there were numerous small peaks from 400–800 nm in the spectra of the SDS-functionalized SWCNTs aqueous solutions. After irradiation for 1 h under 254 nm UV light, the absorption peak for Pd(II) at 420 nm had disappeared completely in the spectrum. This indicates that all of the Pd(II) ions were completely reduced by the photoreduction reaction within 1 h.